

Accelerated scale bridging with sparsely approximated Gaussian learning

Ting Wang^a, Kenneth W. Leiter^a, Petr Plecháč^b, Jaroslaw Knap^a

^a*Simulation Sciences Branch, RDRL-CIH-C, U.S. Army Research Laboratory*

^b*Department of Mathematical Sciences, University of Delaware*

Abstract

Multiscale modeling is a systematic approach to describe the behavior of complex systems by coupling models from different scales. The approach has been demonstrated to be very effective in areas of science as diverse as materials science, climate modeling and chemistry. However, routine use of multiscale simulations is often hindered by the very high cost of individual at-scale models. Approaches aiming to alleviate that cost by means of Gaussian process regression based surrogate models have been proposed. Yet, many of these surrogate models are expensive to construct, especially when the number of data needed is large. In this article, we employ a hierarchical sparse Cholesky decomposition to develop a sparse Gaussian process regression method and apply the method to approximate the equation of state of an energetic material in a multiscale model of dynamic deformation. We demonstrate that the method provides a substantial reduction both in computational cost and solution error as compared with previous methods.

Keywords: Multiscale modeling, Gaussian regression, energetic materials, scale bridging, sparse Cholesky decomposition, gamblets

1. Introduction

Multiscale modeling has now become a *de facto* standard approach for the construction of high-fidelity models of complex phenomena and systems encountered in many areas of science and engineering [1, 2, 3, 4, 5, 6]. The process of building a multiscale model starts with identification of relevant phenomena occurring at individual scales, both spatial and temporal. Thereafter, appropriate at-scale models characterizing these phenomena are selected and combined together into a single multiscale model. Computation is fundamental to multiscale modeling as at-scale models are usually cast in the form of computer models. In recent years, computational aspects of multiscale modeling have become the focal point of numerous research efforts (c.f. [7] for an in-depth review of recent developments). These efforts have led to a conclusion that practicality of multiscale modeling hinges on the ability to significantly reduce the often staggering computational cost of at-scale models. Many different approaches have been proposed in order to reduce this cost, with the vast majority falling under the name of surrogate models. A surrogate model is a cheaper-to-evaluate approximation of a model, constructed from direct observations of the model. Surrogate models have been employed with great success in design optimization [8, 9], where a model is repeatedly evaluated in the search for an

optimal design. In physical sciences, the use of surrogate models can be traced back to the pioneering work of Pope [10], who employed surrogate modeling to enable simulations of combustion chemistry. Other examples of the applications of surrogate models in physical sciences include crystal plasticity [11, 12], elastodynamics [13, 14], atomistic modeling [15, 16], quantum chemistry [17, 18], and fluid dynamics [19]. A comprehensive survey of surrogate modeling techniques, including polynomial regression, kriging, multivariate adaptive regression splines, polynomial stochastic collocation, adaptive stochastic collocation, and radial basis functions can be found in [20, 21].

Gaussian process regression has been advocated as a particularly flexible technique for surrogate model development [22, 23, 16]. However, due to a significant cost of construction, Gaussian process regression is rarely employed to build a single surrogate model. Instead, the domain is often partitioned into a set of subdomains and separate surrogate models are built over each of the subdomains. While such an approach inevitably reduces the overall cost of constructing a surrogate model, this reduction in cost may be accompanied by considerable disadvantages, such as, for example, the loss of smoothness of the surrogate model. In this article, we introduce a methodology to reduce the cost of constructing surrogate models based on Gaussian process regression and apply it in the context of multiscale modeling. We describe the multiscale modeling context of our work in Section 2. The details of our approach are provided in Section 3, along with an application of the technique to constructing a surrogate model of an energetic material in Section 4.

2. A computational framework for scale-bridging in multi-scale simulations

The overarching context of the developments presented in this article is the scale-bridging framework for multiscale modeling of Leiter *et al.* [16]. Here, we only give a brief description of the framework, the reader is referred to [16] for a full exposition. The most elemental multiscale model consists of two at-scale models, the macroscale model F and the microscale model f (c.f. Figure 1). The macroscale model is a mapping $F : I \times D \mapsto R$, where I is a collection of microscale models, domain $D \subset \mathbb{R}^H$, and range $R \subset \mathbb{R}^E$. Similarly, the microscale model is a mapping $f : \hat{D} \mapsto \hat{R}$ where $\hat{D} \subset \mathbb{R}^\eta$ and $\hat{R} \subset \mathbb{R}^\xi$ denote the domain and range of f , respectively. In addition, the framework includes two mappings to transform data between at-scale models. The mapping $G : \tilde{D} \mapsto \hat{D}$, where $\tilde{D} \subset \mathbb{R}^{\tilde{\eta}}$ is the set of intermediate values derived from values in D by F . Henceforth, we refer to G as the “input filter” since it generates the input to f in the set \hat{D} . Likewise, the mapping $g : \hat{R} \mapsto \tilde{R}$, where $\tilde{R} \subset \mathbb{R}^{\tilde{\xi}}$, is referred to as the “output filter” as it extracts relevant data from the microscale model output to be passed to the macroscale model. More complex multiscale models can, of course, be formed through assemblies of multiple two-scale model building blocks.

The centerpiece of the scale-bridging framework is a module coordinating data exchanges between at-scale models, the Evaluation Module (c.f. Figure 2 (a)). The act of sending of $\tilde{\mathbf{u}} \in \tilde{D}$ from F to the Evaluation Module is denoted as an evaluation request. The Evaluation Module carries out five distinct tasks: 1) it collects requests for evaluation of f from F ; 2) it applies the input filter to the evaluation requests to prepare input data for microscale models; 3) it schedules evaluation requests on available resources; 4) it monitors progress of evaluations to detect completion and handle failures; and 5) it

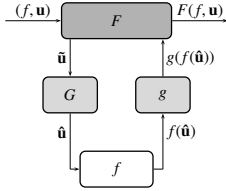


Figure 1: A two-scale model consisting of macroscale model F and microscale model f . Two mappings transform data between scales: the input filter G which transforms data into an appropriate form for the microscale model and the output filter g which extracts relevant data from the microscale model to inform the macroscale model.

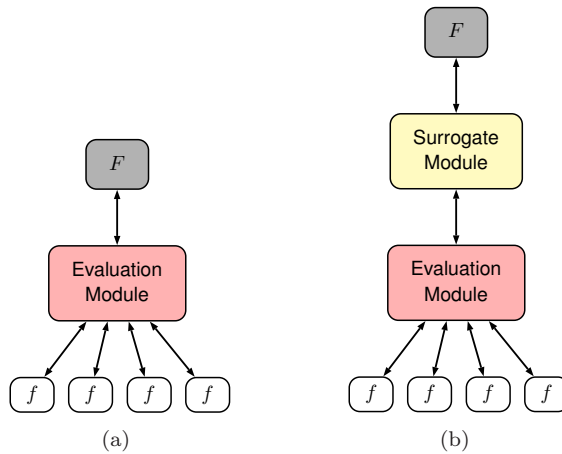


Figure 2: A two-scale model with macroscale model F and microscale model f . (a) The Evaluation Module is inserted as to facilitate evaluations of f required by F . (b) The Surrogate Module is added to adaptively construct a surrogate model for f .

applies the output filter to extract relevant data from completed f evaluations to return to F . However, in many practical applications, microscale models may be extremely costly to evaluate and methods to lower the evaluation cost are necessary in order to render the approach feasible. A popular approach, pioneered by Pope [10] in combustion modeling, relies on adaptive surrogate modeling, where evaluation requests are utilized to on-the-fly build an approximation to the microscale model. Such an approach is particularly advantageous as the modular structure of the scale-bridging framework allows to incorporate surrogate models with ease. Therefore, the framework can be simply augmented by the Surrogate Module operating along side of the macroscale model and the Evaluation Module (c.f. Figure 2 (b)). The role of the Surrogate Module is to automatically construct a surrogate model from completed microscale model evaluation data and subsequently employ the surrogate model in place of microscale model evaluations when appropriate. As a consequence, the use of the surrogate model in the evaluation of the microscale model is fully transparent from the viewpoint of the macroscale model.

The literature dedicated to surrogate modeling is extensive and a thorough survey of surrogate modeling approaches can be found in [20, 21]. In principle, all surrogate

modeling techniques are directly applicable for construction of a surrogate model in the Surrogate Module. However, the Surrogate Model imposes two crucial constraints on the choice of surrogate model. First, an error estimate at new evaluation requests must be available so that the Surrogate Module can choose when to evaluate the surrogate model or the underlying microscale model. Second, the surrogate model must allow for the incorporation of new data acquired from the evaluation of $f(\hat{\mathbf{u}})$ without excessive computational cost. If the computational cost associated with updating the surrogate model is high, the use of the surrogate model may not be advantageous. A particular choice of surrogate modeling satisfying both of the above constraints and advocated by Leiter *et al.* is Gaussian process regression [24]. However, due to the fact that the cost of the Gaussian process regression is dominated by the inversion of the covariance matrix, a single surrogate model over the entire domain \hat{D} of f is not constructed. Instead, a number of independent surrogate models with finite support are constructed within \hat{D} . It bears emphasis that the selection of training points for the construction of these surrogate models is not carried out *a priori*, but instead directly induced by F itself. As a result, the set of all training points within \hat{D} is highly irregular and the set of all surrogate models does not necessarily cover \hat{D} in its entirety. In addition, since individual surrogate models are entirely independent, any notion of global smoothness is absent, leading to complications under the circumstances when global smoothness of approximations to f is required [23]. Yet, despite of these drawbacks, the above surrogate modeling scheme is still capable of yielding remarkable savings in terms of the computational cost, enabling truly extraordinary simulations [16].

3. Accelerated surrogate model

In this section, we describe an approach to substantially reduce the cost of the construction of Gaussian surrogate models. We achieve this goal by leveraging the hierarchical sparse Cholesky decomposition recently developed by Schäfer *et al.* [25] in order to build an approximated global Gaussian surrogate model. Such an approach has two crucial advantages over the approach of Leiter *et al.* [16]. Namely, the global smoothness of approximations to f is guaranteed. Additionally, construction of global surrogate models, i.e. over the entire \hat{D} , is feasible. Hereafter, for simplicity, we focus on a two-scale model in which the microscale model is replaced with an *a priori* constructed surrogate model of the microscale model $\tilde{f}: \hat{D} \mapsto \hat{R}$ (c.f. Figure. 3). We emphasize, however, that the scenario considered here will likely not always be applicable. For example, the microscale model may be composed of two or more microscale models defined over subsets of \hat{D} . Then, one may need to construct separate global surrogate models over each of these subsets. Alternatively, one could construct global surrogate models over some of these subsets and augment them with surrogate models of the type considered in Knap *et al.* [22] and Leiter *et al.* [16]. We do not explore these scenarios in this article, but extensions of our approach to them would be immediate. For the clarity of presentation, we restrict the input dimension of the microscale model to be $\eta = 2$. However, the described approach in this section applies to microscale models with arbitrary input dimensions.

3.1. Gaussian Process Regression

We briefly review the Gaussian process regression in this section. Suppose we have a dataset $\mathcal{D} = (X, Y)$, where $X = (x_1, \dots, x_N)'$ represents a set of N inputs in a domain

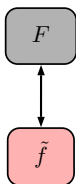


Figure 3: A simplified multiscale framework with the global surrogate model, \tilde{f} , interacting directly with the macroscale model F .

$\Omega \subset \mathbb{R}^2$ and $Y = (y_1, \dots, y_N)'$ represents the corresponding outputs. We aim to build a regression model to interpolate the data set and then use the interpolant to predict at a new set of locations X^* . Gaussian process regression is a popular method for such regression problems [26]. We call a random process $\{f(x)\}_{x \in \Omega}$ a Gaussian process (GP) if for any $n \in \mathbb{Z}_+$, the random vector $(f(x_1), \dots, f(x_n))$ is a n -dimensional Gaussian random vector. The distribution of a GP is completely determined by its mean function $m(x)$ and its covariance function $k(x, x')$ such that

$$m(x) = \mathbb{E}[f(x)] \quad (1)$$

and

$$k(x, x') = \mathbb{E}[(f(x) - m(x))(f(x') - m(x')))]. \quad (2)$$

For simplicity, we assume the GP is centered, i.e., $m(x) = 0$. Hence, a centered GP $\{f(x)\}_{x \in \Omega}$ with covariance function $k(x, x')$ can be written as

$$f(x) \sim \text{GP}(0, k(x, x')).$$

We denote \mathcal{K} the covariance operator that acts on functions such that, for any suitable function g (e.g., $g \in L^2(\Omega)$),

$$(\mathcal{K}g)(x) = \int_{\Omega} k(x, x')g(x') dx'.$$

Often the measurement y at location x contains noise and hence we write

$$y(x) = f(x) + \epsilon,$$

where ϵ is assumed to be iid Gaussian noise $\mathcal{N}(0, \sigma_n^2)$ that is independent with the GP $f(x)$. Thus, the GP model with noisy measurement turns out to be

$$y(x) \sim \text{GP}(0, k_{\sigma_n^2}(x, x')),$$

where $k_{\sigma_n^2}(x, x') = k(x, x') + \sigma_n^2 \delta(x, x')$ and $\delta(x, x')$ is the Dirac function such that $\delta(x, x') = 1$ if $x = x'$ and $\delta(x, x') = 0$ otherwise.

Now given the data set \mathcal{D} , the Gaussian regression treats the prediction at X^* as the mean of the conditional distribution $f(X^*)|\mathcal{D}$. Since the joint distribution of $(Y, f(X^*))$ is a joint Gaussian random vector

$$\mathcal{N}\left(0, \begin{bmatrix} k_{\sigma_n^2}(X, X) & k(X, X^*) \\ k(X^*, X) & k(X^*, X^*) \end{bmatrix}\right),$$

it is straightforward to verify that $f(X^*)|\mathcal{D}$ is still a Gaussian vector with mean

$$\mathbb{E}[f(X^*)|\mathcal{D}] = k(X^*, X)k_{\sigma_n^2}(X, X)^{-1}Y \quad (3)$$

and covariance

$$\text{Cov}[f(X^*)|\mathcal{D}] = k(X^*, X^*) - k(X^*, X)k_{\sigma_n^2}(X, X)^{-1}k(X, X^*). \quad (4)$$

Finally, the mean serves as the prediction of the regression function at locations X^* and the covariance provides a quantification of the prediction uncertainty.

As shown in the formula (3) and (4), GP regression requires the inversion of the dense covariance matrix $K \triangleq k_{\sigma_n^2}(X, X)$, which is often numerically unstable. In practice, one often applies the Cholesky decomposition to K such that $K = LL^T$, where L is a lower triangular matrix. Nevertheless, for a dataset with N observations, the computational complexity of Cholesky decomposition scales as $\mathcal{O}(N^3)$, which becomes computationally prohibitive when $N \gg 1$. Unfortunately, this is the typical case in most multiscale problems where the construction of a high-fidelity surrogate model requires a large number of data. There exist rich literature on reducing the $\mathcal{O}(N^3)$ complexity by approximating the covariance matrix in order to accelerate the Gaussian regression for a large dataset. Most of these approximation methods can be roughly classified into two categories: (1) low rank approximation through subsampling [26] and (2) sparse approximation using inducing variables [27]. Recently, Schäfer *et al.* [25] proposed a novel approximated Cholesky algorithm based on the gamblet transformation [28] which reduces the $\mathcal{O}(N^3)$ bottleneck down to near linear complexity. Moreover, the upper bound of the approximation error can be shown to be exponentially small with respect to some pre-specified parameter. The algorithm, hereafter referred to as the hierarchical sparse Cholesky decomposition algorithm, requires the data points to be approximately equally spaced over the domain Ω , which may limit its application to a general dataset. However, in the context of the multiscale bridging framework, data points from the microscale model can be sampled *a priori* at any location. Hence, we have the flexibility to sample data points over an uniform grid with equal spacing so that the hierarchical sparse Cholesky decomposition algorithm can be applied. In this paper, we aim to build a global Gaussian surrogate model based on the sparse Cholesky decomposition algorithm in order to accelerate the multiscale bridging.

3.2. Gamblets

The theoretical foundation of the hierarchical sparse Cholesky decomposition algorithm relies on the exponential localization property of a set of multi-resolution basis functions called gamblets [28, 29]. We briefly go over the definition of gamblets and its important properties in this section.

Given a centered Gaussian process $\{f(x)\}_{x \in \Omega}$ with kernel $k(x, x')$, we define \mathcal{L} the precision/inversion operator of the covariance operator \mathcal{K} such that, for any suitable function g ,

$$\mathcal{L}\mathcal{K}g(x) = \mathcal{L} \int_{\Omega} k(x, x')g(x') dx' = g(x). \quad (5)$$

The key observation is that the Gaussian process $f(x)$ satisfies the following equation

$$\mathcal{L}f(x) = \Delta(x), \quad (6)$$

where Δ is a centered Gaussian process with covariance operator \mathcal{L} . Also, it can be verified that the kernel k is the Green's function of (6), i.e.,

$$\mathcal{L}k(x, x') = \delta(x, x').$$

Now given a data set $\mathcal{D} = (X, f(X))$, we define a set of basis functions called gamblets,

$$\psi_i(x) = \mathbb{E}[f(x) | f(x_i) = 1 \text{ and } f(x_j) = 0, \forall j \neq i], \quad (7)$$

for $i = 1, \dots, N$, i.e., it is the conditional expectation of $f(x)$ given the observation $f(x_j) = 0$ for all $j \neq i$ and $f(x_i) = 1$. It can be easily verified that the conditional expectation of $f(x)$ given \mathcal{D} is a linear combination of the gamblets

$$\mathbb{E}[f(x) | \mathcal{D}] = \sum_{i=1}^N f(x_i) \psi_i(x).$$

This is saying that the best “guess” of $f(x)$ given the dataset \mathcal{D} is a linear combination of the observed features $f(x_1), \dots, f(x_N)$ if all the gamblets are known. The following two properties of gamblets are crucial for deriving the hierarchical sparse Cholesky algorithm.

- **Representation:** Each gamblet function admits the following representation in terms of the covariance kernel k ,

$$\psi_i(x) = \sum_{j=1}^N K_{ij}^{-1} \int_{\Omega} k(x, y) \delta(x_j, y) dy, \quad (8)$$

where K^{-1} is the inverse of the covariance matrix $K = k(X, X)$.

- **Exponential localization:** The gamblet functions are exponentially decaying in the sense that

$$|\langle \mathcal{L}\psi_i, \psi_j \rangle| \leq C e^{-\beta d(x_i, x_j)} \quad (9)$$

for some constants $C, \beta > 0$, where $\langle f, g \rangle = \int_{\Omega} f(x)g(x) dx$ is the L^2 -inner product and $d(x, y)$ is some distance between x and y . This property provides the theoretical foundation to sparsely approximate the dense covariance matrix.

3.3. Multi-resolution gamblets and block Cholesky decomposition

In this section, we provide a heuristic derivation for the hierarchical sparse Cholesky decomposition. The algorithm assumes that the configuration of the input set are nested with q levels. For ease of presentation, throughout of this section we set $q = 2$ so that the two-level input set $X = X^{(2)}$ forms an uniform grid of resolution 2^{-2} over the domain $\Omega = [0, 1] \times [0, 1]$. The two-level input set $X^{(2)}$ can be obtained by subdividing the level-one grid $X^{(1)}$, where $X^{(1)}$ is the set of input points that forms the uniform grid with resolution 2^{-1} (c.f. Figure 4). Similarly, the q -level uniform grid with resolution 2^{-q} can be obtained by recursively subdividing Ω for q times. We denote $I^{(1)}$ and $I^{(2)}$ the index sets of points in $X^{(1)}$ and $X^{(2)}$ respectively. That is, $x_i \in X^{(l)}$ whenever $i \in I^{(l)}$ for $l = 1, 2$. We henceforth write $x_i^{(l)}$ to emphasize the fact that x_i is a point in $X^{(l)}$. Clearly, $I^{(1)}$ is a subset of $I^{(2)}$ and hence we can define the index set $J^{(1)} = I^{(1)}$ and

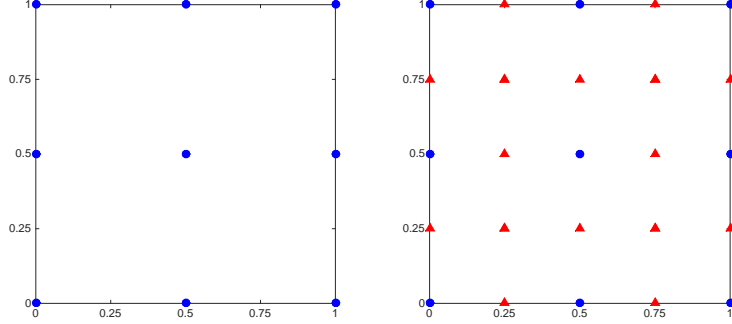


Figure 4: Configuration of dataset over $[0, 1] \times [0, 1]$. Left: the one-level uniform grid $X^{(1)}$ with resolution 2^{-1} . Right: the two-level uniform grid $X^{(2)}$ with resolution 2^{-2} . The index set $I^{(1)}$ contains the index of the blue dots and index set $I^{(2)}$ contains the index of both the blue dots and red triangles. The index set $J^{(1)}$ contains the index of the blue dots and the index set $J^{(2)}$ contains the index of the red triangles.

$J^{(2)} = I^{(2)}/I^{(1)}$, i.e., $J^{(2)}$ contains the index of those data points that are in $X^{(2)}$ but not in $X^{(1)}$. Hence, we can classify the points in $X^{(2)}$ into two categories: $X_{J^{(1)}}^{(2)} = X^{(1)}$ contains level two points that are also in level one and $X_{J^{(2)}}^{(2)} = X^{(2)}/X^{(1)}$ contains points that are in level two but not in level one.

The above recursive sampling procedure can be viewed as a two-step hierarchical sampling approach, where a fine dataset $\mathcal{D}^{(2)} = (X^{(2)}, f(X^{(2)}))$ is sampled on top of the coarse dataset $\mathcal{D}^{(1)} = (X^{(1)}, f(X^{(1)}))$. Now given the datasets $\mathcal{D}^{(1)}$ and $\mathcal{D}^{(2)}$, we denote by

$$K^{(1)} = k\left(X^{(1)}, X^{(1)}\right)$$

and

$$K^{(2)} = k\left(X^{(2)}, X^{(2)}\right)$$

their corresponding covariance matrices. Following the definition of gamblers in (7), we can define the level one and level two gamblers by

$$\psi_i^{(1)}(x) = \mathbb{E}\left[f(x) \mid f(x_i^{(1)}) = 1 \text{ and } f(x_j^{(1)}) = 0, \forall j \neq i \in I^{(1)}\right]$$

and

$$\psi_i^{(2)}(x) = \mathbb{E}\left[f(x) \mid f(x_i^{(2)}) = 1 \text{ and } f(x_j^{(2)}) = 0, \forall j \neq i \in I^{(2)}\right],$$

respectively. Using the definition of operator \mathcal{L} and the representation (8), it can be readily shown that the following two matrices

$$B^{(1)} = \left[\langle \mathcal{L}\psi_i^{(1)}, \psi_j^{(1)} \rangle\right]_{i,j \in I^{(1)}}$$

and

$$B^{(2)} = \left[\langle \mathcal{L}\psi_i^{(2)}, \psi_j^{(2)} \rangle\right]_{i,j \in I^{(2)}}.$$

are the inverse of the covariance matrices $K^{(1)}$ and $K^{(2)}$ respectively. Hence, hereafter we refer $B^{(l)}$ as the precision matrix associated with the dataset $\mathcal{D}^{(l)}$ for $l = 1, 2$. It is immediate that each precision matrix is exponentially localized (i.e., nearly sparse) due to the exponential localization of gamblers. Let us write the precision matrix $B^{(2)}$ in a block matrix form (corresponding to sets $X_{J^{(1)}}^{(2)}$ and $X_{J^{(2)}}^{(2)}$)

$$B^{(2)} = \begin{bmatrix} B_{11}^{(2)} & B_{12}^{(2)} \\ B_{21}^{(2)} & B_{22}^{(2)} \end{bmatrix}.$$

To be consistent, we also write the level one precision matrix $B^{(1)}$ as a single block matrix

$$B^{(1)} = B_{11}^{(1)}.$$

Owhadi and Scovel [28, 30] have proved that for a wide range of kernel functions k , the conditional numbers of the block matrices $B_{11}^{(1)}$ and $B_{22}^{(2)}$ are bounded. Based on this fact, they have further shown that the inverses matrices $B_{11}^{(1),-1}$ and $B_{22}^{(2),-1}$ are exponentially localized as well.

With the above preparations, now we are ready to motivate the hierarchical sparse Cholesky decomposition algorithm. We start by making an important observation that links block Cholesky decomposition (or LDL^T decomposition) with the two level hierarchical sampling procedure that we illustrated above. Recall that $K^{(2)}$ is the covariance matrix associated with the two-level dataset $\mathcal{D}^{(2)}$. Its block Cholesky decomposition (corresponding to $X_{J^{(1)}}^{(2)}$ and $X_{J^{(2)}}^{(2)}$) reads

$$K^{(2)} = \begin{bmatrix} I & 0 \\ K_{21}^{(2)} & K_{11}^{(2),-1} \end{bmatrix} \begin{bmatrix} K_{11}^{(2)} & 0 \\ 0 & K_{22}^{(2)} - K_{21}^{(2)} K_{11}^{(2),-1} K_{12}^{(2)} \end{bmatrix} \begin{bmatrix} I & K_{11}^{(2),-1} K_{12}^{(2)} \\ 0 & I \end{bmatrix}, \quad (10)$$

where $K_{i,j}^{(2)}$ is the covariance matrix between $X_{J^{(i)}}^{(2)}$ and $X_{J^{(j)}}^{(2)}$. Since $K^{(2)}$ is the inverse of the precision matrix $B^{(2)}$, basic linear algebra shows that

$$K_{21}^{(2)} K_{11}^{(2),-1} = -B_{22}^{(2),-1} B_{21}^{(2)} = \left[\langle \delta(x_i^{(2)}, \cdot), \psi_j^{(1)} \rangle \right]_{i \in J^{(2)}, j \in J^{(1)}} \quad (11)$$

and the Schur complement

$$K_{22}^{(2)} - K_{21}^{(2)} K_{11}^{(2),-1} K_{12}^{(2)} = B_{22}^{(2),-1} = \left[\langle \mathcal{L}\psi_i^{(2)}, \psi_j^{(2)} \rangle \right]_{i,j \in J^{(2)}}. \quad (12)$$

Hence the block Cholesky decomposition of $K^{(2)}$ can be rewritten in terms of $B^{(2)}$ as

$$\begin{aligned} K^{(2)} &= \begin{bmatrix} I & 0 \\ -B_{22}^{(2),-1} B_{21}^{(2)} & I \end{bmatrix} \begin{bmatrix} B_{11}^{(1),-1} & 0 \\ 0 & B_{22}^{(2),-1} \end{bmatrix} \begin{bmatrix} I & -B_{12}^{(2)} B_{22}^{(2),-1} \\ 0 & I \end{bmatrix} \\ &= \begin{bmatrix} L_{11}^{(1)} & 0 \\ -B_{22}^{(2),-1} B_{21}^{(2)} & L_{22}^{(2)} \end{bmatrix} \begin{bmatrix} L_{11}^{(1),T} & -B_{12}^{(2)} B_{22}^{(2),-1} \\ 0 & L_{22}^{(2),T} \end{bmatrix}, \end{aligned} \quad (13)$$

where $L_{11}^{(1)}$ and $L_{22}^{(2)}$ are the Cholesky factors of $B_{11}^{(1),-1}$ and $B_{22}^{(2),-1}$ respectively, i.e.,

$$B_{11}^{(1),-1} = L_{11}^{(1)} L_{11}^{(1),T}$$

and

$$B_{22}^{(2),-1} = L_{22}^{(2)} L_{22}^{(2),T}.$$

An application of Cauchy-Schwarz inequality to (11) shows that the off-diagonal part of the Cholesky factor is exponentially localized. Furthermore, the result (Theorem 3.12) in [25] shows that the block Cholesky factors $L_{11}^{(1)}$ and $L_{22}^{(2)}$ are also exponentially localized. This suggests that the entire Cholesky factor in (13) is exponentially localized. In other words, up to exponentially small entries, the Cholesky factor of $K^{(2)}$ is nearly sparse and the sparsity pattern is known a priori. Therefore, it is desirable to skip the exponentially small entries in the process of Cholesky factorization in order to reduce the computational complexity, which leads to the basic idea of the hierarchical sparse Cholesky decomposition.

3.4. The sparse GP algorithm

The above heuristic derivation is based on a dataset over a two-level uniform grid. However, the same argument can be easily extended for a dataset over a q level uniform grid by successively doing the block Cholesky decomposition (13) for $q - 1$ times, which leads to the block Cholesky decomposition

$$K^{(q)} = L^{(q)} L^{(q),T}.$$

Since the locations (row and column) of those exponentially small entries in $L^{(q)}$ are explicitly known, with a certain confidence level, we can sparsely approximate $L^{(q)}$ by replacing these entries by zero. Schäfer *et al.* [25] define the set of sparsity pattern to be

$$\mathcal{S}_R = \left\{ (i, j) \in I^{(q)} \times I^{(q)} \mid i \in J^{(k)}, j \in J^{(l)}, |x_i - x_j| \leq R2^{-k \wedge l} \right\},$$

where R is a parameter that controls the level of sparsity. Then they suggest to restrict the Cholesky computation only to this sparsity set through applying the zero fill-in incomplete Cholesky decomposition [31] to the sparse matrix

$$K_R^{(q)}(i, j) = \begin{cases} K^{(q)}(i, j) & \text{for } (i, j) \in \mathcal{S}_R \\ 0 & \text{otherwise,} \end{cases} \quad (14)$$

such that $K_R^{(q)} \approx L_R^{(q)} L_R^{(q),T}$. Here the incomplete Cholesky factor $L_R^{(q)}$ is obtained by stepping through the Cholesky reduction on $K_R^{(q)}$ setting $L_R^{(q)}(i, j)$ to zero if the corresponding $K_R^{(q)}(i, j)$ is zero. Finally, the main result in [25] asserts that we can use $L_R^{(q)} L_R^{(q),T}$ to approximate the original dense covariance matrix $K^{(q)}$ such that

$$\left\| K^{(q)} - L_R^{(q)} L_R^{(q),T} \right\| \leq p(N) e^{-\gamma R} \quad (15)$$

for some constant γ and polynomial $p(N)$, where the constant γ is independent of q . Moreover, the computational complexity for obtaining $L_R^{(q)}$ is $\mathcal{O}(N \log^2(N) R^4)$, which is near linear in N . Hence, the sparsity parameter R controls the trade-off between efficiency and accuracy. With larger R , the error bound is decreased but the complexity is increased. Finally, the sparse GP algorithm that uses the hierarchical sparse Cholesky decomposition for Gaussian regression is as follows.

Algorithm 1 Sparse GP on an uniform grid of level q

- 1: **procedure** SPARSEGP($\mathcal{D}^{(q)}$)
 - 2: Order the data points from $J^{(1)}$ to $J^{(q)}$ (coarse to fine)
 - 3: Initialize $K_R^{(q)}(i, j) = K^{(q)}(i, j)$ if $(i, j) \in S_R$ and $K_R^{(q)}(i, j) = 0$ otherwise
 - 4: $L_R^{(q)} \leftarrow \text{IncompleteChol}(K_R^{(q)})$ ▷ Incomplete Cholesky decomposition
 - 5: $\alpha = L_R^{(q),T} \setminus L_R^{(q)} \setminus Y$ ▷ Backward substitution and then forward substitution
 - 6: $v = L_R^{(q)} \setminus k(X^{(q)}, X^*)$
 - 7: $\mathbb{E}[f(X^*) | \mathcal{D}^{(q)}] = k(X^{(q)}, X^*)^T \alpha$ ▷ Update the predictive mean
 - 8: $\text{Cov}[f(X^*) | \mathcal{D}^{(q)}] = k(X^*, X^*) - v^T v$ ▷ Update the predictive variance
-

A few comments are in order: (1) Note that the above algorithm is simply the standard Gaussian regression with the Cholesky decomposition of $K^{(q)}$ replaced by the incomplete Cholesky of its sparse approximation $K_R^{(q)}$. Hence, the algorithm can be easily implemented on top of the standard GP algorithm. (2) It is important that the input points $X^{(q)}$ in the dataset are order from $J^{(1)}$ to $J^{(q)}$ for the algorithm to work correctly. In the case that the data are not sample in this order, we can identify a permutation matrix P such that PKP^T has the correct ordering. (3) Our presentation of Algorithm 1 assumes that the configuration of the input set is strictly uniform over the domain Ω . However, we point out that this is requirement can be relaxed. Indeed, the algorithm is robust as long as the input configuration satisfies some certain criteria (c.f. [25] for more details).

4. Results

We now assess the sparse GP method in the context of a computationally demanding multiscale model of impact physics. The multiscale model consists of two at-scale models, a continuum mechanics macroscale model and a particle-based microscale model. The surrogate model serves to replace evaluation of the microscale model at a significantly reduced computational cost. The new sparse GP method is compared with the adaptive sampling based approach of Leiter *et al.* [16], summarized below, which constructs individual surrogate models on subsets of the entire training dataset.

4.1. Macroscale model

The macroscale model is a continuum mechanics model of a deforming body implemented in the ALE3D multi-physics finite-element code [32]. The material of the body is taken to be the energetic 1,3,5-trinitrohexahydro-s-triazine (RDX) and its equation of state (EOS) is obtained through evaluation of the microscale model. The EOS provides the pressure, p , and temperature, T , for a given mass density, ρ , and internal energy density, e . The macroscale model uses a modified predictor-corrector algorithm to integrate energy forward in time. The predictor step includes the pressure volume work over the first half of the timestep plus strain work from the deviatoric stress: $\tilde{e} = e_t - \frac{1}{2}p_t dV + de_{dev}$, where e_t is the energy density at the start of the timestep, p_t is the pressure at the start of the timestep, dV is the change in relative volume over the timestep, and de_{dev} is the change in deviatoric strain energy density. The deviatoric strain energy is computed using a conventional J_2 -plasticity model with Steinberg-Guinan

hardening [33] with a yield strength of 150 MPa, hardening coefficient of 200 and hardening exponent of 0.1. The predictor pressure and temperature are computed using the EOS as

$$p_p = p(\rho_{t+1}, \tilde{e}) \quad (16)$$

$$T_p = T(\rho_{t+1}, \tilde{e}) \quad (17)$$

where ρ_{t+1} is the mass density at the end of the timestep. The corrector step updates the energy as $e_{t+1} = \tilde{e} - \frac{1}{2}p_p dV$ giving the pressure and temperature at the end of the step as

$$p_{t+1} = p(\rho_{t+1}, e_{t+1}) \quad (18)$$

$$T_{t+1} = T(\rho_{t+1}, e_{t+1}) \quad (19)$$

At modest pressures, the energy update in the corrector step is small, which leads to a small change in pressure. In order to avoid a second EOS evaluation per timestep, the pressure and temperature corrections are omitted in our approach. The energy is updated, but the temperature and pressure updates lag behind:

$$p_{t+1} = p_p \quad (20)$$

$$T_{t+1} = T_p \quad (21)$$

$$e_{t+1} = \tilde{e} - \frac{1}{2}p_p dV \quad (22)$$

4.2. Microscale model

The microscale model computes the EOS using energy-conserving dissipative particle dynamics (DPD). The simulations are managed by the LAMMPS Integrated Materials Engine (LIME), a Python wrapper to LAMMPS that automates EOS evaluation [34]. LIME initializes and equilibrates a simulation cell containing 21,952 particles (28 x 28 x 14 unit cells) of RDX to be consistent with the prescribed mass density and energy density. Following equilibration, the temperature and pressure of the system are computed via ensemble averages.

4.3. Adaptive sampling

The adaptive sampling method reduces computational cost of expensive multiscale models. We refer the reader to Knap *et al.* [22] and Leiter *et al.* [16] for a detailed description of the adaptive sampling algorithm and its implementation in the scale-bridging framework, but will briefly describe the method here. Adaptive sampling is an active learning algorithm that constructs a set of local GP surrogate models on-the-fly to replace the evaluation of computationally expensive microscale models. In the case of the multiscale model considered here, the surrogate models approximate the EOS computed using DPD. While the macroscale model integrates its solution forward in time, it repeatedly evaluates the EOS. With adaptive sampling, the EOS is either evaluated by a surrogate model or by the microscale model. An error estimate of the

surrogate model for a particular ρ and e is compared to a user-specified acceptable error tolerance parameter, \tilde{e}_{tol} , to determine if the EOS evaluation is satisfied by the surrogate model. If the error estimate is too high, the EOS is computed by the microscale model and the result is used to update the surrogate model. The adaptive sampling algorithm continuously improves the accuracy of the surrogate model for regions of the EOS of interest to the macroscale model. The number of data to be incorporated into a surrogate model may be potentially very large, especially for low values of \tilde{e}_{tol} . The computational cost of GP regression scales as $\mathcal{O}(N^3)$ where N is the number of data. Rather than construct a single GP surrogate model across all of the data, the adaptive sampling algorithm builds a number of local GP surrogate models on a partition of the overall data. A parameter d_{max} determines the maximum number of data per local surrogate model. The collection of surrogate models is stored in a metric-tree database to allow quick access for evaluation and update.

Although adaptive sampling has been very successful in reducing computational cost of expensive multiscale models [22, 11, 16] it suffers two significant drawbacks in practice: 1) the patchwork collection of local GP surrogate models gives no guarantee of continuity between the patches; 2) the overall simulation is often highly load imbalanced due to the unpredictable adaptive execution of expensive microscale models.

4.4. Taylor impact simulation

We compare the performance of the sparse GP method and the adaptive sampling method for the simulation of a Taylor impact experiment, commonly used to characterize the deformation behavior of materials [35]. The simulation setup is identical to the one in [16]. In a Taylor impact experiment, a cylinder of material travels at a constant initial velocity and impacts a rigid anvil. In the simulations presented here, the cylinder of RDX has a height of 1.27 cm and radius of 0.476 cm and travels at 200 m/s. In the macroscale model, axisymmetry is imposed along the cylinder axis and the cylinder is decomposed into 1600 first-order quadrilateral elements. We simulate the impact for 20 μs using an adaptive timestep with the initial timestep set to 0.001 μs and the maximum allowable timestep set to 0.012 μs for a total of 1,676 timesteps. The simulations are executed on the SGI ICE X high performance computer "Topaz" at the Engineering Research and Development Center.

For simulations that use the sparse GP method, only a single compute node, containing a 36 core 2.3 GHz Intel Xeon Haswell processor, is used because all of the microscale model data is precomputed. The microscale model is computed for values of e between -1.0×10^7 J/m³ and 1.7×10^8 J/m³ and for ρ between 1.75 g/cm³ and 1.93 g/cm³. The bounds are selected based upon previous experience running the simulation. The requirement to select appropriate bounds for the grid sampling is a drawback of the sparse GP method compared to the adaptive sampling method, which is able to expand the sampling region during model evaluation on-demand. Two sets of microscale model data are obtained corresponding to $q = 6$ and $q = 7$, for a total of 4,225 and 16,641 points respectively. For each level q , three Taylor impact simulations are performed under different values of the sparsity parameter R : $R = 6, 8, \text{ and } 10$ for $q = 6$ and $R = 8, 10, \text{ and } 12$ for $q = 7$. The squared exponential kernel

$$k_{\sigma_n^2}(x, x') = \sigma_f^2 \exp\left(\frac{-|x - x'|^2}{2l^2}\right) + \sigma_n^2 \delta(x, x')$$

q	R	Sparsity	Wall-Clock Time (hr)	Hyperparameter Opt. Time (hr)	Compute Time (hr)	# Microscale Model Evals
6	6	0.74	0.9	0.6	11,504	4,225
6	8	0.64	1.5	0.8	11,525	4,225
6	10	0.54	2.7	1.5	11,561	4,225
7	8	0.85	11.4	8.8	44,345	16,641
7	10	0.80	18.4	15.3	44,570	16,641
7	12	0.74	40.9	32.3	45,274	16,641

Table 1: Timing data for simulations with sparse GP surrogate models. The sparsity is the fraction of non-zero entries in the original covariance matrix $K^{(q)}$ that are replaced by zeros in the sparse covariance matrix $K_R^{(q)}$. The wall-clock time is for the execution of the simulation and includes the optimization of the hyperparameters. The compute time includes both the time required to precompute the microscale model at sampling points and for the execution of the simulation.

is used for the GP, where the hyperparameter l is the length-scale, σ_f^2 is the signal variance and σ_n^2 is the noise variance. The choice of the squared exponential kernel reflects our prior belief that the microscale model outputs are smooth and hence we seek a smooth approximation. Hyperparameters for the sparse GP surrogate model are obtained by minimizing the negative log marginal likelihood (NLML) with the BFGS algorithm implemented in the dlib C++ toolkit [36] using a stopping criterion of 10^{-3} . The starting point for the hyperparameter optimization is chosen to be $l = 0.2$, $\sigma_f^2 = 1.0$, and $\sigma_n^2 = 0.01$.

Simulations employing the adaptive sampling method are executed on a total of 90 compute nodes for a total of 3,240 cores. The macroscale model and adaptive sampling module are executed on a single node, with the remaining 89 compute nodes dedicated to microscale model evaluations. The maximum number of points per local surrogate model, d_{max} is chosen to be 50. Three simulations are performed under different \tilde{e}_{tot} : 10^{-2} , 5×10^{-3} , and 2×10^{-3} .

The results of the adaptive sampling and sparse GP simulations are compared to those of a reference simulation computing the microscale DPD model for all EOS evaluations of the macroscale model. The reference simulation requires a total of 2,681,600 microscale model evaluations and completes in 32.05 days of wall-clock time on 12,852 processor cores for a total compute time of 9,885,192 hours.

4.5. Results

Timing data for Taylor impact simulations with the sparse GP surrogate model are presented in Table 1. Here the sparsity is the fraction of non-zeros in the covariance matrix $K^{(q)}$ that are replaced by zeros in the sparse covariance matrix $K_R^{(q)}$ (c.f. (14)). The compute time includes the time required to evaluate the microscale model for input points of grid level q , the time to optimize the hyperparameters of the model, and the time to execute the Taylor impact simulation. The compute time to sample the microscale model at grid points is 11,475 hr for $q = 6$ and 43,980 hr for $q = 7$. This indicates that for all simulations with the sparse GP surrogate model, the vast majority of total compute time, greater than 95%, is spent sampling the microscale model. We note, however, that sampling the microscale model incurs a one-time expense for a

\tilde{e}_{tol}	Wall-Clock Time (hr)	Compute Time (hr)	# Microscale Model Evals
10^{-2}	2.3	7,546	833
5×10^{-3}	8.7	28,315	1,878
2×10^{-3}	156.3	506,333	27,827
No Surrogate Module	769.2	9,885,192	2,681,600

Table 2: Timing data for simulations with adaptive sampling. The wall-clock time is for the execution of the simulation, which includes the on-demand evaluation of the microscale model and update of the collection of surrogate models according to the adaptive sampling algorithm. The compute time is for the execution of the simulation, which for adaptive sampling includes the microscale model evaluation.

particular q and the data can be reused across multiple simulations. In addition, the sampling points are nested across levels, which allows some microscale model data to be reused from lower q levels. Obtaining microscale model results at sampling points is embarrassingly parallel as all points are chosen ahead of time for a particular value of q . Given sufficient computing resources, the microscale model data can be obtained in a very short amount of wall-clock time. Therefore, the wall-clock time given in Table 1 omits time spent precomputing the microscale model and includes only the time to optimize hyperparameters, dependent on the choice of R , and the time required to complete the Taylor impact simulation. A significant portion of the wall-clock time, ranging from 50% to 83% is spent on optimization of the hyperparameters. The remaining time is spent on evaluation of the surrogate model and the integration of the macroscale model forward in time.

For comparison, we present timing data in Table 2 for simulations that use adaptive sampling. A detailed discussion of these timings can be found in [16]. It should be noted here that both the adaptive sampling method and the sparse GP method allow for simulations that are orders of magnitude cheaper than the benchmark simulation which always obtains the EOS from the microscale model.

We now assess the effect of grid level q and sparsity parameter R on the solution of the Taylor impact problem. In Figure 5, we plot the L_2 -norm of the error in the displacements predicted by the macroscale model as a function of simulation time for sparse GP simulations with $q = 6$. For comparison, we also plot the error for the adaptive sampling simulations with \tilde{e}_{tol} of 10^{-2} , 5×10^{-3} and 2×10^{-3} . The L_2 -norm of the error in the displacements field \mathbf{u} is:

$$\|\mathbf{u}^{surr} - \mathbf{u}^{ref}\|_2 = \left(\int_V \sum_{i=1}^3 |u_i^{surr}(v) - u_i^{ref}(v)|^2 dv \right)^{1/2} \quad (23)$$

where $u_i^{surr}(v)$ is the i -th component of the the displacements field obtained from the simulation employing a surrogate model, $u_i^{ref}(v)$ is the i -th component of the field from the reference simulation, and V denotes the volume of the cylinder.

As R is increased, the error in displacements is reduced. The sparse GP simulation with $q = 6$ and $R = 8$ has an error roughly equivalent to the adaptive sampling simulation with $\tilde{e}_{tol} = 5 \times 10^{-3}$, but uses only 17% of the wall-clock time and 41% the compute time. The simulation with $q = 6$ and $R = 10$ has a lower error than the adaptive sampling

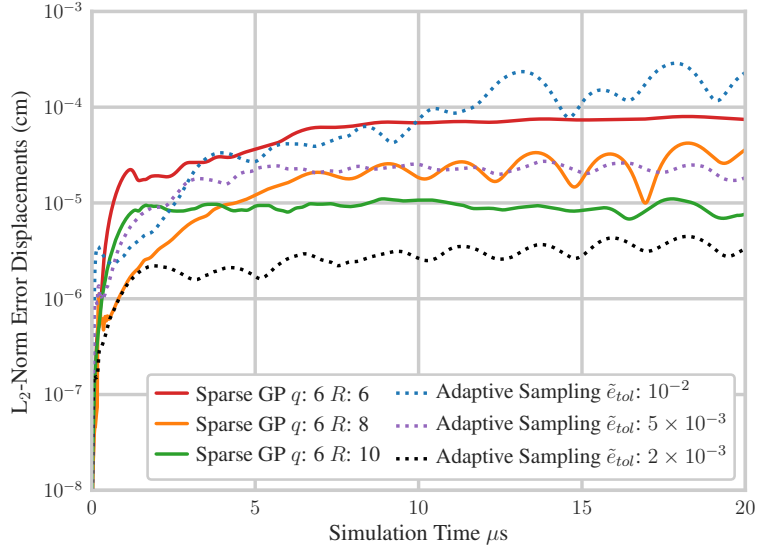


Figure 5: Error in displacements for three Taylor impact simulations with a sparse GP surrogate model with $q = 6$ and $R = 6, 8,$ and 10 and for three simulations using adaptive sampling with $\tilde{e}_{tol} = 10^{-2}, 5 \times 10^{-3},$ and 2×10^{-3}

simulation with $\tilde{e}_{tol} = 5 \times 10^{-3}$, but requires only 31% of the wall-clock time and 41% of the compute time. These results demonstrate that the sparse GP method provides a more accurate solution than the adaptive sampling method at a fraction of the wall-clock and simulation time.

For $q = 6$, the number of microscale model evaluations is 4,225, which is more than twice as many as used in the adaptive sampling simulation with $\tilde{e}_{tol} = 5 \times 10^{-3}$. It may appear surprising that the cost of the sparse GP simulations, in terms of both wall-clock time and compute time, are less than those using adaptive sampling despite the many more microscale model evaluations used. However, the reduction in cost is completely a consequence of the computational load imbalance inherent in the adaptive sampling method that is not present when using the sparse GP surrogate model. In adaptive sampling, many processors are left underutilized during long stretches of the simulation due to the unpredictable on-demand evaluation of microscale models, a major drawback to the method. In the sparse GP approach, all microscale model data is precomputed ahead of time and is perfectly scalable and computationally efficient. Computational resources are also fully utilized throughout the simulation itself, spent primarily on the evaluation of the EOS using the surrogate model.

None of the sparse GP simulations with $q = 6$ reduce the error below that obtained using adaptive sampling with the lowest $\tilde{e}_{tol} = 2 \times 10^{-3}$. Further simulations with $q = 6$ and values of R beyond 10, not included here, provide no further reduction in the error. To determine whether the error of sparse GP simulations can be reduced further by increasing the amount of microscale model data available, the error in the displacements field for sparse GP simulations with $q = 7$ is plotted in Figure 6. In fact, the error is reduced further by using a higher q . As was the case with $q = 6$, increasing R reduces the

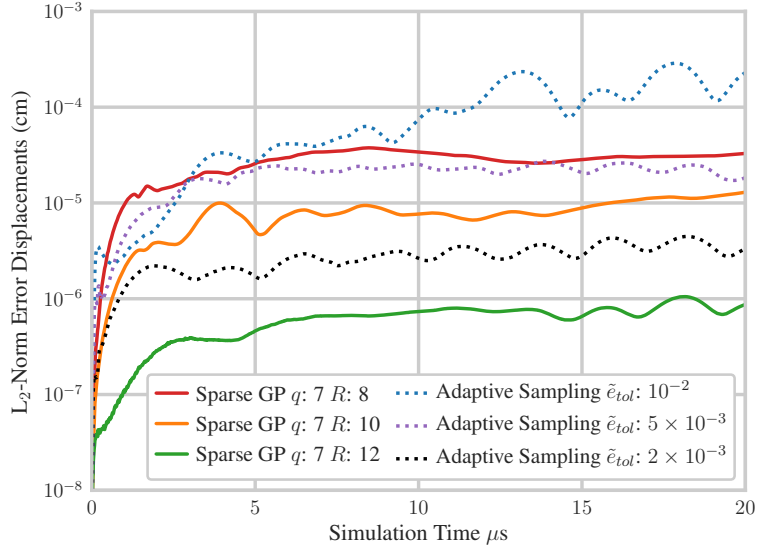


Figure 6: Error in displacements for three Taylor impact simulations with a sparse GP surrogate model with $q = 7$ and $R = 8, 10$, and 12 and for three simulations using adaptive sampling with $\tilde{\epsilon}_{tol} = 10^{-2}, 5 \times 10^{-3}$, and 2×10^{-3}

error in the solution. The sparse GP simulation with $q = 7$ and $R = 12$ provides an error in displacements well below the smallest error obtained using adaptive sampling with $\tilde{\epsilon}_{tol} = 2 \times 10^{-3}$ and is able to achieve the reduced error with 26% of the wall-clock time and 9% of the compute time, a significant improvement. Furthermore, the sparse GP surrogate model uses many fewer microscale model evaluations, only 16,641, compared to the 27,827 microscale model evaluations required by the most accurate adaptive sampling simulation. This is especially strong evidence of the advantage of the sparse GP method. Given even fewer samples of the microscale model, the sparse GP method produces a more accurate surrogate model than adaptive sampling.

One interesting comparison can also be made between two of the sparse GP simulations, one with parameters $q = 6$ and $R = 8$ and another with $q = 7$ and $R = 8$. Both simulations have roughly the same error in the solution, despite the increase in microscale model data available for the $q = 7$ simulation run. This observation can be explained by the error bound (15). For sparse GP with $q = 7$, the polynomial term $p(N)$ in the error bound may be significantly larger than that of the sparse GP with $q = 6$, which offsets the higher accuracy provided by the finer sampling. This indicates that when less accuracy is required, a good strategy may be to avoid over sampling the microscale model as a coarse sampling should be sufficient.

5. Summary

In this article, we have described a formulation of a sparse GP regression method based on the near linear complexity sparse Cholesky algorithm of Schäfer *et al.* [25]. The sparse GP method is capable of utilizing a large number of training data and, thus,

avoiding a bottleneck associated traditionally with GP methods. This behavior is due to the fact that the dense covariance matrix admits an approximate sparse Cholesky decomposition, which reduces the computational $\mathcal{O}(N^3)$ complexity down to near linear in N . In addition, the sparse GP method provides error bounds for the sparse approximation that are exponentially small with respect to a chosen sparsity parameter.

Subsequently, we have employed the sparse GP method to construct a surrogate model for a microscale model in a two-scale model of deformation of an energetic material. The microscale model characterizes the volumetric response of the energetic material by recourse to dissipative particle dynamics. In turn, the macroscopic model is a finite-element model simulating dynamic deformation. We have considered two scenarios: 1) the evaluation of the microscale model is replaced by an adaptive sampling approach, amounting to on-the-fly construction of GP surrogates with compact support; 2) the evaluation of the microscale model is replaced by a sparse GP surrogate model constructed over the entire domain of the microscale model. We have contrasted these two scenarios in terms of the overall computational cost required to construct the surrogate models and perform simulations with the macroscopic model.

Our results indicate that the sparse GP surrogate model offers remarkable computational savings over the adaptive sampling surrogate model. In some cases, these savings translate into over 10-fold reduction in terms of the computational cost. This reduction is primarily due to the fact that the sparse GP surrogate model relies on a fixed grid for the selection of sampling points and the sampling can be easily carried out with an extraordinary level of concurrency. Of course, appropriate bounds for the extents of the grid must be selected *a priori* as to guarantee that all evaluations requested by the macroscopic model will ultimately be fully contained within the grid. We emphasize that the adaptive sampling surrogate model does not suffer from such a limitation as it is constructed adaptively and can incorporate data from any subset of the domain. However, in practice, good estimates for the bounds may be easily available from, for example, lower fidelity microscale models.

In addition to the computational savings offered by the sparse GP method, it also leads to a greater accuracy in the displacement field than the local GP models constructed in the adaptive sampling method. The increase in accuracy of the sparse GP method is likely because it takes into account the long range correlations between data points, which are not included when the data is partitioned into separate GP surrogates with compact support.

It should be pointed out that the EOS regression problem showcased here is low dimensional and that additional methods will be required to extend GP regression to high dimensions, such as active subspaces [37] or additive kernels [38]. Sparse GP regression helps to alleviate the problem of high dimensionality somewhat by enabling the incorporation of more data into the surrogate model. Perhaps combining dimension reduction methods with the sparse GP method outlined here could address even higher dimensional problems and is a subject of ongoing research.

6. Acknowledgements

The authors would like to thank Dr. Rich Becker of the U.S. Army Research Laboratory and Florian Schäfer of Caltech for fruitful discussions. The work of T.W. and P.P.

was supported in part by the DARPA project W911NF-15-2-0122. This work was supported in part by a grant of computer time from the DoD High Performance Computing Modernization Program at the U.S. Army Engineer Research and Development Center.

References

References

- [1] W. A. Curtin, R. E. Miller, Atomistic/continuum coupling in computational materials science, *Modelling and Simulation in Materials Science and Engineering* 11 (3) (2003) R33.
- [2] F. Pelupessy, A. van Elteren, N. de Vries, S. McMillan, N. Drost, S. P. Zwart, The astrophysical multipurpose software environment, *Astronomy & Astrophysics* 557 (2013) A84.
- [3] V. S. Mahadevan, E. Merzari, T. Tautges, R. Jain, A. Obabko, M. Smith, P. Fischer, High-resolution coupled physics solvers for analysing fine-scale nuclear reactor design problems, *Philosophical Transactions of the Royal Society of London A: Mathematical, Physical and Engineering Sciences* 372 (2021).
- [4] J. L. Suter, D. Groen, P. V. Coveney, Chemically specific multiscale modeling of clay-polymer nanocomposites reveals intercalation dynamics, tactoid self-assembly and emergent materials properties, *Advanced Materials* 27 (6) (2015) 966–984.
- [5] P. Perdikaris, L. Grinberg, G. E. Karniadakis, Multiscale modeling and simulation of brain blood flow, *Physics of Fluids* 28 (2) (2016) 021304.
- [6] S. Alowayyed, D. Groen, P. V. Coveney, A. G. Hoekstra, Multiscale computing in the exascale era, *Journal of Computational Science* 22 (2017) 15 – 25.
- [7] D. Groen, J. Knap, P. Neumann, D. Suleimenova, L. Veen, K. Leiter, Mastering the scales: a survey on the benefits of multiscale computing software, *Philosophical Transactions A*, (in print).
- [8] G. G. Wang, S. Shan, Review of metamodeling techniques in support of engineering design optimization, *Journal of Mechanical Design* 129 (4) (2007) 370–380.
- [9] S. Koziel, D. E. Ciaurri, L. Leifsson, Surrogate-based methods, in: *Computational Optimization, Methods and Algorithms*, Springer Berlin Heidelberg, 2011, Ch. 3, pp. 33–59.
- [10] S. Pope, Computationally efficient implementation of combustion chemistry using in situ adaptive tabulation, *Combustion Theory and Modelling* 1 (1) (1997) 41–63.
- [11] N. R. Barton, J. Knap, A. Arsenlis, R. Becker, R. D. Hornung, D. R. Jefferson, Embedded polycrystal plasticity and adaptive sampling, *International Journal of Plasticity* 24 (2) (2008) 242–266.
- [12] H. F. Alharbi, S. R. Kalidindi, Crystal plasticity finite element simulations using a database of discrete fourier transforms, *International Journal of Plasticity* 66 (2015) 71 – 84.
- [13] B. Rouet-Leduc, K. Barros, E. Cieren, V. Elango, C. Junghans, T. Lookman, J. Mohd-Yusof, R. S. Pavel, A. Y. Rivera, D. Roehm, A. L. McPherson, T. C. Germann, Spatial adaptive sampling in multiscale simulation, *Computer Physics Communications* 185 (7) (2014) 1857 – 1864.
- [14] D. Roehm, R. S. Pavel, K. Barros, B. Rouet-Leduc, A. L. McPherson, T. C. Germann, C. Junghans, Distributed database kriging for adaptive sampling (D2KAS), *Computer Physics Communications* 192 (2015) 138–147.
- [15] Z. Li, J. R. Kermode, A. De Vita, Molecular dynamics with on-the-fly machine learning of quantum-mechanical forces, *Physical Review Letters* 114 (2015) 096405.
- [16] K. W. Leiter, B. C. Barnes, R. Becker, J. Knap, Accelerated scale-bridging through adaptive surrogate model evaluation, *Journal of Computational Science* 27 (2018) 91–106.
- [17] M. Rupp, A. Tkatchenko, K.-R. Müller, O. A. von Lilienfeld, Fast and accurate modeling of molecular atomization energies with machine learning, *Phys. Rev. Lett.* 108 (2012) 058301.
- [18] R. Gómez-Bombarelli, J. N. Wei, D. Duvenaud, J. M. Hernández-Lobato, B. Sanchez-Lengeling, D. Sheberla, J. Aguilera-Iparraguirre, T. D. Hirzel, R. P. Adams, A. Aspuru-Guzik, Automatic chemical design using a data-driven continuous representation of molecules, *ACS Central Science* 4 (2) (2018) 268–276.
- [19] L. Zhao, Z. Li, B. Caswell, J. Ouyang, G. E. Karniadakis, Active learning of constitutive relation from mesoscopic dynamics for macroscopic modeling of non-newtonian flows, *Journal of Computational Physics* 363 (2018) 116 – 127.
- [20] R. Jin, W. Chen, T. Simpson, Comparative studies of metamodeling techniques under multiple modelling criteria, *Structural and Multidisciplinary Optimization* 23 (1) (2001) 1–13.

- [21] O. Sen, S. Davis, G. Jacobs, H. Udaykumar, Evaluation of convergence behavior of metamodeling techniques for bridging scales in multi-scale multimaterial simulation, *Journal of Computational Physics* 294 (2015) 585–604.
- [22] J. Knap, N. R. Barton, R. D. Hornung, A. Arsenlis, R. Becker, D. R. Jefferson, Adaptive sampling in hierarchical simulation, *International Journal for Numerical Methods in Engineering* 76 (4) (2008) 572–600.
- [23] N. R. Barton, J. V. Bernier, J. Knap, A. J. Sunwoo, E. K. Cerreta, T. J. Turner, A call to arms for task parallelism in multi-scale materials modeling, *International Journal for Numerical Methods in Engineering* 86 (6) (2011) 744–764.
- [24] C. E. Rasmussen, C. K. I. Williams, *Gaussian Processes for Machine Learning (Adaptive Computation and Machine Learning)*, MIT Press, 2005.
- [25] F. Schäfer, T. J. Sullivan, H. Owhadi, Compression, inversion, and approximate pca of dense kernel matrices at near-linear computational complexity, arXiv preprint arXiv:1706.02205.
- [26] C. E. Rasmussen, Gaussian processes in machine learning, in: *Advanced lectures on machine learning*, Springer, 2004, pp. 63–71.
- [27] J. Quiñonero-Candela, C. E. Rasmussen, A unifying view of sparse approximate gaussian process regression, *Journal of Machine Learning Research* 6 (Dec) (2005) 1939–1959.
- [28] H. Owhadi, Multigrid with rough coefficients and multiresolution operator decomposition from hierarchical information games, *SIAM Review* 59 (1) (2017) 99–149.
- [29] H. Owhadi, Bayesian numerical homogenization, *Multiscale Modeling & Simulation* 13 (3) (2015) 812–828.
- [30] H. Owhadi, C. Scovel, Universal scalable robust solvers from computational information games and fast eigenspace adapted multiresolution analysis, arXiv preprint arXiv:1703.10761.
- [31] G. H. Golub, C. F. Van Loan, *Matrix computations*, Vol. 3, JHU Press, 2012.
- [32] A. Anderson, R. Cooper, R. Neely, A. Nichols, R. Sharp, B. Wallin, Users manual for ALE3D—an arbitrary Lagrange/Eulerian 3D code system, LLNL, Version 3 (1).
- [33] D. J. Steinberg, S. G. Cochran, M. W. Guinan, A constitutive model for metals applicable at high-strain rate, *Journal of Applied Physics* 51 (3) (1980) 1498–1504.
- [34] B. C. Barnes, K. W. Leiter, R. Becker, J. Knap, J. K. Brennan, LAMMPS integrated materials engine (LIME) for efficient automation of particle-based simulations: application to equation of state generation, *Modelling and Simulation in Materials Science and Engineering* 25 (5) (2017) 055006.
- [35] G. Taylor, The use of flat-ended projectiles for determining dynamic yield stress. I. Theoretical considerations, *Proceedings of the Royal Society of London A: Mathematical, Physical and Engineering Sciences* 194 (1038) (1948) 289–299.
- [36] D. E. King, Dlib-ml: A machine learning toolkit, *Journal of Machine Learning Research* 10 (2009) 1755–1758.
- [37] R. Tripathy, I. Bilonis, M. Gonzalez, Gaussian processes with built-in dimensionality reduction: Applications to high-dimensional uncertainty propagation, *Journal of Computational Physics* 321 (2016) 191 – 223.
- [38] D. K. Duvenaud, H. Nickisch, C. E. Rasmussen, Additive gaussian processes, *Advances in Neural Information Processing Systems* 24 (2011) 226–234.